PUBLISHED VERSION

Coherence imaging of scrape-off-layer and divertor impurity flows in the Mega Amp Spherical Tokamak (invited)
Silburn S A, Harrison J R, Howard J, Gibson K J, Meyer H, Michael C A, Sharples R M

© 2014 UNITED KINGDOM ATOMIC ENERGY AUTHORITY

This article may be downloaded for personal use only. Any other use requires prior permission of the author and the American Institute of Physics. The following article appeared in Proceedings of the 20th Topical Conference on High-Temperature Plasma Diagnostics, Atlanta, Georgia, USA, June 2014. Review of Scientific Instruments, Vol.85, No.11, November 2014, pp.11D703 and may be found at: http://dx.doi.org/10.1063/1.4891165

AIP | Review of Scientific Instruments

Coherence imaging of scrape-off-layer and divertor impurity flows in the Mega Amp Spherical Tokamak (invited)a)

S. A. Silburn, J. R. Harrison, J. Howard, K. J. Gibson, H. Meyer, C. A. Michael, and R. M. Sharples

Citation: Review of Scientific Instruments **85**, 11D703 (2014); doi: 10.1063/1.4891165
View online: http://dx.doi.org/10.1063/1.4891165
View Table of Contents: http://scitation.aip.org/content/aip/journal/rsi/85/11?ver=pdfcov
Published by the AIP Publishing

Articles you may be interested in

Snowflake divertor configuration studies in National Spherical Torus Experimenta)
Phys. Plasmas **19**, 082504 (2012); 10.1063/1.4737117

Generation of non-axisymmetric scrape-off layer perturbations for controlling tokamak edge plasma profiles and stabilitya)
Phys. Plasmas **19**, 056124 (2012); 10.1063/1.3702048

High density Langmuir probe array for NSTX scrape-off layer measurements under lithiated divertor conditionsa)
Rev. Sci. Instrum. **81**, 10E117 (2010); 10.1063/1.3494381

Doppler coherence imaging and tomography of flows in tokamak plasmas (invited)a)
Rev. Sci. Instrum. **81**, 10E528 (2010); 10.1063/1.3492422

Advanced tokamak research with integrated modeling in JT-60 Upgradea)
Phys. Plasmas **17**, 056112 (2010); 10.1063/1.3327917

This article is copyrighted as indicated in the article. Reuse of AIP content is subject to the terms at: http://scitationnew.aip.org/termsconditions. Downloaded to IP: 194.81.223.66 On: Tue, 16 Sep 2014 10:01:54

Coherence imaging of scrape-off-layer and divertor impurity flows in the Mega Amp Spherical Tokamak (invited)[a)]

S. A. Silburn,[1,b)] J. R. Harrison,[2] J. Howard,[3] K. J. Gibson,[4] H. Meyer,[2] C. A. Michael,[2,c)] and R. M. Sharples[1]

[1]*Centre for Advanced Instrumentation, Department of Physics, Durham University, Durham DH1 3LE, United Kingdom*
[2]*CCFE, Culham Science Centre, Abingdon, Oxon OX14 3DB, United Kingdom*
[3]*Plasma Research Laboratory, Australian National University, Canberra, ACT 0200, Australia*
[4]*York Plasma Institute, Department of Physics, University of York, Heslington, York YO10 5DD, United Kingdom*

(Presented 3 June 2014; received 4 June 2014; accepted 12 July 2014; published online 1 August 2014)

A new coherence imaging Doppler spectroscopy diagnostic has been deployed on the UK's Mega Amp Spherical Tokamak for scrape-off-layer and divertor impurity flow measurements. The system has successfully obtained 2D images of C III, C II, and He II line-of-sight flows, in both the lower divertor and main scrape-off-layer. Flow imaging has been obtained at frame rates up to 1 kHz, with flow resolution of around 1 km/s and spatial resolution better than 1 cm, over a 40° field of view. C III data have been tomographically inverted to obtain poloidal profiles of the parallel impurity flow in the divertor under various conditions. In this paper we present the details of the instrument design, operation, calibration, and data analysis as well as a selection of flow imaging results which demonstrate the diagnostic's capabilities. © *2014 AIP Publishing LLC*. [http://dx.doi.org/10.1063/1.4891165]

I. INTRODUCTION

Impurity ion flows in the scrape-off-layer (SOL) and divertor regions of tokamak plasmas have important implications for particle and heat exhaust control in current and future devices.[1] To design and operate effective exhaust solutions for these devices requires an understanding of the flow physics and the development of predictive numerical models; these efforts in turn require the support of high quality experimental flow data.

Coherence Imaging Spectroscopy (CIS) is a recently developed diagnostic technique which can produce wide field-of-view, 2D images of impurity flows via Doppler shifts of ion emission lines using an imaging interferometer. Under suitable symmetry constraints the data can be tomographically inverted to obtain 2D impurity emissivity and flow profiles suitable for detailed comparison with modelling.[2] Since this technique can provide orders of magnitude more spatial information than typical dispersive Doppler spectroscopy instruments, overall flow patterns and behaviour can be much more readily interpreted from the resulting images.

In this paper we present details of, and selected results from, a new CIS impurity flow diagnostic on the Mega Amp Spherical Tokamak (MAST). This diagnostic was operated throughout the 2013 experimental campaign, to image flows of intrinsic C^+, C^{2+}, and He^+ impurities in both the main SOL and lower divertor.

II. MEASUREMENT PRINCIPLE

The theory of operation of Doppler CIS diagnostics has been discussed in detail in Refs. 3 and 4 so here we present only a simplified illustration of how Doppler shifts are measured with the technique.

Consider the plasma light to be analysed traversing a 2-beam interferometer, which splits the light 50:50 and introduces a time delay τ_0 between the two beams arriving at the detector. In the simple case of monochromatic emission with optical frequency ν_0, the signal at the interferometer output is a sinusoidal fringe pattern:

$$S(\tau_0) = \frac{I_0}{2}(1 + \zeta \cos(2\pi \nu_0 \tau_0)), \tag{1}$$

where I_0 is the source brightness and ζ is the "fringe contrast," equal to 1 for this idealised case. A shift in the observed emission frequency $\Delta\nu$ will change the phase of the cosine in Eq. (1) by a corresponding amount $\Delta\phi = 2\pi\,\Delta\nu\tau_0\kappa$, where κ is a correction to account for any frequency dependence of τ_0 (i.e., dispersion).[5] Writing the un-shifted phase as $\phi_0 = 2\pi\nu_0\tau_0$, we find a simple relationship between changes in the fringe phase and Doppler shifts:

$$\frac{\Delta\phi}{\kappa\phi_0} = \frac{\Delta\nu}{\nu_0} \approx \frac{\boldsymbol{v}.\hat{\boldsymbol{l}}}{c}, \tag{2}$$

where $\boldsymbol{v}$ is the emitter velocity and $\hat{\boldsymbol{l}}$ is the observation line-of-sight direction.

In spatial heterodyne CIS, an imaging 2-beam interferometer applies a fixed phase delay ϕ_0 at all positions in a 2D image of the plasma. An additional delay is then added which varies along one image direction, $\phi_s(y)$. The effect of this position-dependent delay is to produce a set of parallel

[a)]Invited paper, published as part of the Proceedings of the 20th Topical Conference on High-Temperature Plasma Diagnostics, Atlanta, Georgia, USA, June 2014.
[b)]Electronic mail: s.a.silburn@durham.ac.uk
[c)]Present address: Plasma Research Laboratory, Australian National University, Canberra, ACT 0200, Australia.

 © 2014 AIP Publishing LLC

This article is copyrighted as indicated in the article. Reuse of AIP content is subject to the terms at: http://scitationnew.aip.org/termsconditions. Downloaded to IP: 194.81.223.66 On: Tue, 16 Sep 2014 10:01:54

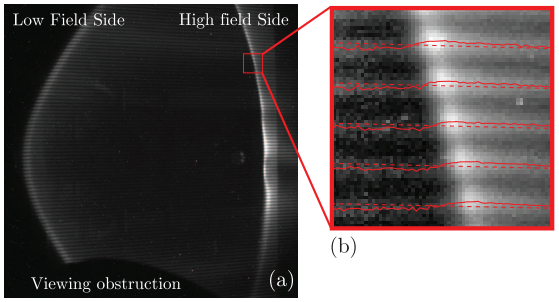

FIG. 1. (a) Raw camera image showing a tangential view of an H-mode double null divertor MAST plasma, filtered for C III 465 nm. C III emission can be seen localised at the edge of the plasma. (b) Magnified and contrast enhanced section of the raw image at the high field side, showing the shape of the fringes distorted due to Doppler shifts (solid lines) compared to the undistorted pattern (dashed lines). Bright speckles on the image are caused by neutrons interacting with the un-shielded camera.

interference fringes superimposed on the image (Fig. 1(a)). Phase changes $\Delta\phi$ due to spatially varying Doppler shifts then manifest as distortions of this parallel fringe pattern, which are measured by comparing the plasma images to the un-distorted (calibration) fringe pattern using FFT techniques (Fig. 1(b)). The difference between the two at each point gives the flow information for that location. This scheme allows 2D spatial and spectral information to be captured simultaneously on a 2D detector, so that the time resolution is only limited by the detector framing rate. Note that while each image column gives essentially independent flow information, in the vertical direction we effectively only have one fully independent measurement per fringe. The spatial resolution in the vertical direction is therefore limited by the scale of the fringes ($\approx$12 pixels for the MAST instrument), and the system should be configured such that the maximum resolution lies along the direction where the strongest flow gradients are expected.

III. HARDWARE

Following Doppler CIS instruments used on other devices,[2,6] the MAST instrument uses a static polarisation-based interferometer, in which orthogonal polarisation states act as the two interferometer beams and share a common physical beam path. This makes the system compact, easy to align, and relatively robust to mechanical disturbance. A schematic of the optical system is shown in Fig. 2. First an F-Mount zoom lens l_1 views the plasma through a diagnostic port and forms a demagnified plasma image. The light is then collimated by placing this image at the detector plane of a second camera lens l_2 with its focus set to infinity. This arrangement allows easy adjustment of the instrument field of view between 9° and 40° using the zoom control of l_1. At the widest field of view each pixel corresponds to 1.5 mm in the plasma cross-section.

The interferometer components are mounted in a custom temperature stabilised enclosure in the collimated region after l_2. The temperature stabilisation reduces delay drifts caused by thermal expansion and thermo-optic effects in the interferometer components. First is a linear polariser with its polarisation axis vertical in the x, y plane. This is followed by a

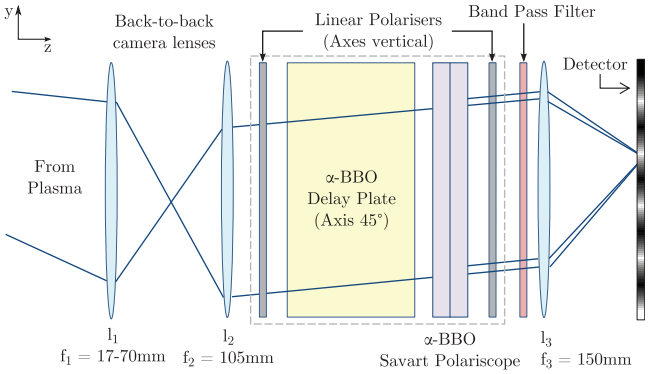

FIG. 2. Simplified schematic of the MAST CIS optical system.

thick birefringent alpha barium borate (α-BBO) plate ("delay plate"), with its optic axis in the x, y plane and rotated 45° with respect to the polariser axis. The plate's birefringence causes a delay ϕ_0 between the (equal amplitude) beam components polarised parallel and perpendicular to its optic axis (i.e., ±45° from vertical), determined by the material birefringence and plate thickness. The next component is an α-BBO Savart polariscope: a type of polarising beam splitter[7] which introduces a small vertical displacement between the orthogonally polarised beam components. When imaged through the final lens l_3, this beam displacement causes an angle-dependent geometrical path difference which creates the horizontal fringe pattern ϕ_s. The final interferometer component is a second linear polariser with its axis parallel to the first, which allows the two orthogonally polarised beams to interfere at the detector.

Following the interferometer components, a third camera lens l_3 focused at infinity forms the final image at the detector. A 3-cavity band pass interference filter is mounted to this lens to isolate the ion line of interest from the plasma spectrum. The detector used is a Photron APX-RS high speed camera which uses a 1024×1024, 10-bit CMOS detector capable of frame rates up to 3 kHz. The maximum frame rate used on MAST was limited to 1 kHz by the available photon flux.

The complete system occupies a space envelope of 84 cm × 23 cm × 22 cm (L × W × H), and is sufficiently portable to be moved between different diagnostic ports to access different plasma views. A photograph of the instrument in the lab is shown in Fig. 3. The plasma views used in this paper are shown in Fig. 4: a wide angle view of the lower divertor and a radial view of the centre column from the vertical midplane.

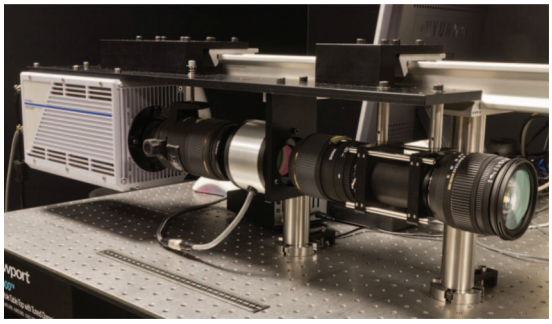

FIG. 3. Photograph of the MAST CIS diagnostic set up for testing in the lab, next to a 30 cm ruler for scale.

This article is copyrighted as indicated in the article. Reuse of AIP content is subject to the terms at: http://scitationnew.aip.org/termsconditions. Downloaded to IP: 194.81.223.66 On: Tue, 16 Sep 2014 10:01:54

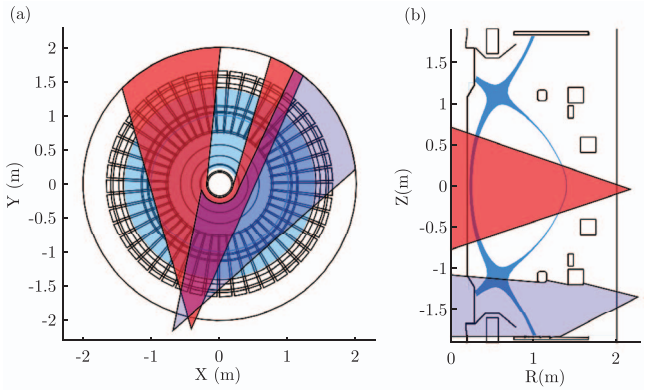

FIG. 4. Viewing cones for the radial midplane and lower divertor plasma views, viewing the tokamak from above (a) and side-on (b).

The instrument was designed to be configurable for either the C III 464.9 nm triplet, C II 514.2 nm multiplet, or He II 468.6 nm multiplet. These are the brightest visible impurity lines on MAST thus enabling the highest frame rates, and allow measurements in multiple charge:mass ratio species and access to different (overlapping) spatial regions in the plasma (e.g., C II emission was observed to peak up to 4 cm further from the separatrix in the divertor legs than C III, while He II is dominant near and above the X-point). Fig. 5 shows measured line profiles of the C III and He II lines in the MAST divertor, with the transmission curves of their respective line selection filters over-plotted. Optimising the filter and imaging lens specifications to ensure adequate separation of these lines over the entire field of view, while also maximising throughput and minimising vignetting through the multiple camera lens configuration, was the main driver in the optical design. Transmission band shifts for light incident obliquely on the filter are controlled by limiting the off-axis beam angles in the collimated region to $<5^\circ$.

The interferometer group delay $\kappa\phi_0$ was chosen to optimise flow measurements for the targeted spectral lines. Equation (2) shows that larger delays give a greater sensitivity of the fringe phase to flows. However, this neglects variation of the fringe contrast ζ with delay, which lowers the fringe signal-to-noise ratio for finite width spectral lines. In accordance with the Wiener–Khinchin theorem, it can be shown that ζ is in fact related to the Fourier transform of the spectral line shape.[5] Note that due to this line shape sensitivity, the contrast varies with ion temperature for Doppler broadened lines and can be used as a T_i diagnostic.[3,6,8] However, this complicates the interpretation of the fringe phase images, thus to optimise for flow measurements we choose a delay where the contrast is relatively insensitive to T_i. Based on modelling of ζ for the measured multiplet line structures, a delay plate thickness of $L = 6.5$ mm was chosen as a good compromise between maximising ζ, maximising the phase sensitivity to flows, and minimising T_i sensitivity for all three spectral lines. This thickness is expected to give a delay of $\kappa\phi_0 \approx 2000$ waves for the C III and He II lines and $\approx$1700 waves for C II, calculated from the Sellmeier equations for α-BBO.[9] Additional delay plates with $L = 4.6$ mm and 9.8 mm were also used, primarily to investigate fringe contrast behaviour and for further consistency checks which will not be discussed here.

IV. CALIBRATION

From Sec. II, it can be seen that accurate flow measurements require the delay $\kappa\phi_0$ to be well known, and for a zero-flow fringe pattern reference to be obtained. One-off calibration of $\kappa\phi_0$ has been performed by imaging a diffuser illuminated by a tunable diode laser. For each delay plate, images were captured for a laser tuning range $\Delta\nu/\nu_0$ equivalent to a Doppler shift $\approx$1–10 km/s in the vicinity of 460.9 nm. For each recorded image the fringe shift $\Delta\phi$ (relative to the first image in the sequence) was averaged over the central 512×512 region of the detector to obtain a single phase shift value for each tuning step. From Eq. (2), $\Delta\phi$ is expected to vary linearly with the fractional change in laser frequency with a gradient of $\kappa\phi_0$. The calibration results are shown in Fig. 6. The results show the expected linear relationship, and the values of $\kappa\phi_0$ for each delay plate were determined from linear fits to the data (solid lines). These were found to be approximately 5% larger than expected from the α-BBO Sellmeier equations, however this does not significantly affect the optimisation of ζ for the 6.5 mm plate. These measured delay values are used for the plasma data analysis, after adjusting for the difference in wavelength between these results and the plasma ion lines.

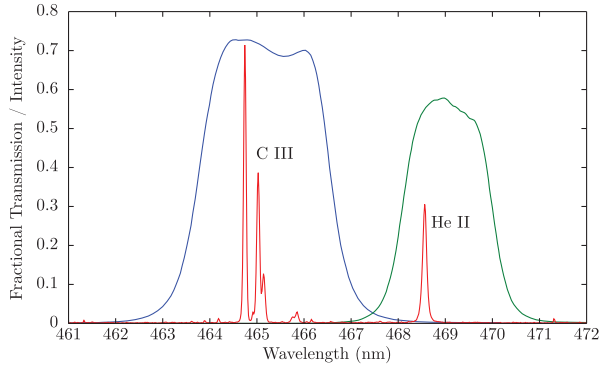

FIG. 5. Measured spectra of the C III 465 nm triplet and He II 469 nm multiplet on MAST, and the line selection filters

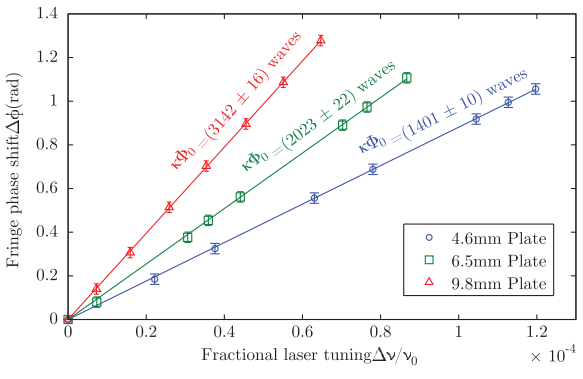

FIG. 6. Calibration of the group delay $\kappa\phi_0$ using a tunable laser: measured fringe phase as a function of laser tuning (points) and corresponding linear fits (solid lines).

This article is copyrighted as indicated in the article. Reuse of AIP content is subject to the terms at: http://scitationnew.aip.org/termsconditions. Downloaded to IP: 194.81.223.66 On: Tue, 16 Sep 2014 10:01:54

To obtain a reference for the un-distorted fringe pattern directly, a source of each ion spectral line without Doppler shift is required. In practice such sources are not available, and instead nearby spectral lamp lines (Cd I 467.8 nm for the He II and C III plasma lines, and Cd I 508.6 nm for the C II line) are used. Images are captured in the laboratory with the spectral lamp illuminating a 15 cm integrating sphere to fill the field of view and collection solid angle of the instrument. These are demodulated as described in Sec. V to obtain a reference phase image. In order to reduce the effects of image noise on the calibration, the phase images are fit with a 3rd order bivariate polynomial in pixel coordinates x, y, and the fitted phase image used as the reference. Scaling of the phase image is also performed to account for the wavelength difference between the lamp and plasma lines.

In practice it was found that the reference phase calibration could only be obtained to within a spatially constant phase offset using this method, i.e., the shape of the fringe pattern could be calibrated but an unknown shift of the entire pattern remained. The result is a systematic offset of the zero point of the measurements. Despite the temperature stabilisation, the phase delay ϕ_0 also drifts with ambient temperature due to thermal effects in the main delay plate, causing a slow drift of the calibration offset. Drifts of up to 16 km/s have been observed over a week long period. Because this offset is constant across the image, however, the correct flow value need only be known at one image location to fully constrain the calibration. This was achieved by identifying pixels whose sight-lines view the plasma radially (e.g., straight towards the centre column for the midplane view), and are expected to show almost zero line-of-sight flow. The calibration is then adjusted to set the mean flow value of these pixels to zero.

In addition to the above interferogram calibrations, flat field intensity images were obtained with a calibrated integrating sphere in order to calibrate the absolute light sensitivity of the system, and enable correction for vignetting in the plasma images.

V. DATA ANALYSIS

Demodulation to extract brightness and phase images from the camera output is performed column-wise on the raw images. After filtering the image to remove detector hot pixels and bright spots caused by neutrons hitting the un-shielded camera, the underlying brightness for each image column is extracted using frequency-domain filtering to remove the horizontal fringes. The brightness is then factored out of the raw column data leaving only the sinusoidal fringe pattern, and the fringe phase at each pixel is found from the phase of the complex discrete time "analytic" signal for the data column, calculated using a FFT based technique.[10] For plasma data, the reference phase image is then subtracted to leave only the phase shift $\Delta\phi(x, y)$. Flow images are obtained from this using Eq. (2). As will be discussed below, the flow calculated in this way represents a weighted "line-of-sight average" flow. Nevertheless, such images are very useful for visualising and qualitatively interpreting flow phenomena. For quantitative comparisons with modelling, tomographic inversion of the results is required.

The simple analysis leading to Eq. (2) assumes that the spectrum at each image point describes a single value of flow. However, when viewing a real plasma the spectrum describes a range of flow speeds along the camera line-of-sight. It can be shown[2] that the flow calculated using Eq. (2), which we will now denote $\bar{v}$, represents a line-average of the local flow $\boldsymbol{v}(\boldsymbol{r})$ along the line of sight L, weighted by the local emissivity $e_0(\boldsymbol{r})$:

$$\bar{v} \approx \frac{1}{I_0}\int_L e(\boldsymbol{r})\boldsymbol{v}(\boldsymbol{r})\cdot \boldsymbol{dl}. \tag{3}$$

Here I_0 is the line-integrated emissivity,

$$I_0 = \int_L e(\boldsymbol{r})dl. \tag{4}$$

Since $\boldsymbol{v}(\boldsymbol{r})$ and $e_0(\boldsymbol{r})$ are also time dependent quantities, the measurements will represent a time average over the camera exposure (1–20 ms for the MAST CIS system). Techniques to invert camera data in the form of Eq. (4) to obtain poloidal profiles of emissivity are well established. However, inverting Eq. (3) to obtain the local flow is more challenging since the integral is weighted by both the local emissivity and the local direction of the flow relative to the line-of-sight. The local emissivity weightings can be determined by first inverting (4) so that $e(\boldsymbol{r})$ is known. To deal with the dot product, we assume the flow is primarily along the magnetic field lines, i.e., $\boldsymbol{v}(\boldsymbol{r})\cdot\boldsymbol{dl} \approx v_{||}(\boldsymbol{r})\hat{\boldsymbol{B}}(\boldsymbol{r})\cdot\boldsymbol{dl}$. The field direction $\hat{\boldsymbol{B}}(\boldsymbol{r})$ is obtained from magnetic equilibrium reconstruction using the EFIT code, allowing the weighting due to the dot product to be calculated.

Both the emissivity and flow images are inverted using an iterative procedure based on the simultaneous algebraic reconstruction technique (SART),[11] with the constraints of toroidal symmetry and non-negativity of the emissivity. In order to reduce the memory requirements of the inversions, the intensity and flow images are usually binned to 256×256 pixels before being inverted on to a 1 cm × 1 cm resolution grid in the R, Z plane. This results in an overdetermined tomography problem, with the number of data pixels usually more than twice the number of grid cells. Image demodulation and tomographic inversion have been implemented in MATLAB, with processing of a single raw image to obtain inverted brightness and flow profiles taking typically 2–3 min on a laptop computer.

VI. RESULTS AND DISCUSSION

The Doppler CIS diagnostic was operated throughout the most recent experimental campaign on MAST, obtaining data for all three targeted impurity species at frame rates between 50 Hz to 1 kHz depending on ion species, view, and plasma conditions. The estimated flow ($\bar{v}$) resolution achieved was typically around 1 km/s, primarily set by the fringe signal-to-noise ratio which depends on the image brightness and fringe contrast. We now briefly present a selection of flow imaging results which illustrate the capabilities of the CIS diagnostic.

Using the radial midplane view illustrated in Fig. 4, novel field-aligned C III flow patterns have been observed under specific conditions at the high field side of many MAST

This article is copyrighted as indicated in the article. Reuse of AIP content is subject to the terms at: http://scitationnew.aip.org/termsconditions. Downloaded to IP: 194.81.223.66 On: Tue, 16 Sep 2014 10:01:54

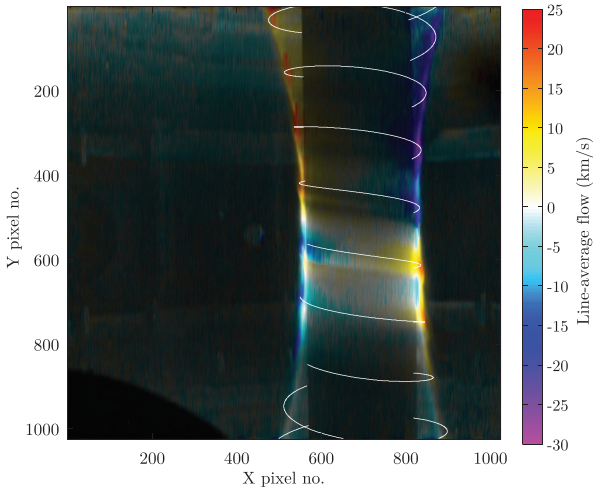

FIG. 7. Line-integrated emissivity (image brightness) and line average C III flow (color) for shot 28 749 from a 5 ms exposure between 125 and 129 ms. A magnetic field line from EFIT is projected as a solid white line on the image.

plasmas. An example intensity (I_0) and line-average flow ($\bar{v}$) image is shown in Fig. 7, where the brightness of the image represents I_0 and the color represents $\bar{v}$. Flow away from the camera (red-shift) is designated positive. The MAST centre column is visible just off-centre of the image, with C III emission localised near the centre column at the inboard edge of the plasma. Around the centre column, stripes with opposite flow directions can be seen in the lower part of the plasma. This is in the early phase of a double-null divertor (DND) discharge, when the plasma is transitioning from being limited on the centre column to a diverted configuration, while being fuelled by gas puffing from the centre column at the midplane. The flow pattern is well aligned with the equilibrium magnetic field line pitch (a field line from EFIT is shown in Fig. 7 as a solid white line). Based on this, the image is interpreted as showing oppositely directed C III flows along neighbouring field lines. This phenomenon has been observed almost ubiquitously in DND plasmas with the combination of inboard midplane gas fuelling and an inner radius very close to the centre column. Near the vertical centre of the image fine radial structure is seen in the flows, and the flow direction along the highlighted field line is reversed above and below the midplane. While the physics giving rise to this pattern is still under investigation, these results demonstrate the advantages of the CIS technique for revealing flow patterns which would otherwise be very difficult to diagnose from a small number of chordal measurements.

Using a series of repeated lower single null divertor (LSND) plasmas with plasma current $I_p = 600$ kA and 1.2 MW of neutral beam injection (NBI) auxiliary heating, divertor flows of each impurity species have been recorded in matched plasma conditions. The discharge featured periods of L-mode, edge localised mode (ELM) free H-mode, and Type I ELMy H-mode operation. Representative I_0 and $\bar{v}$ images for the L-mode and ELM free H-mode periods are shown in Fig. 8, with the divertor view corresponding to that shown in Fig. 4. Each image is an average over approximately 16 ms and has been binned to 256×256 pixels after demodulation. White areas at the divertor strike points in He II indicate a

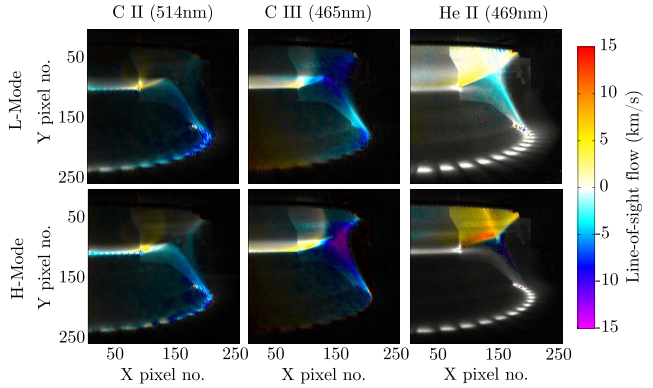

FIG. 8. Line-integrated emission and line-average flow images for C II, C III, and He II in the divertor of repeated LSND plasma shots. Each image is integrated over a period of 16 ms. Top row: images during L-mode and bottom row: during ELM-free H-mode.

lack of flow information, due to spectral contamination of the He II line at these locations. Horizontal striping in the flow images also appears along the inner strike point for the Carbon species; this is an artifact caused by the intensity varying over spatial scales smaller than the fringes on the raw images. For all species, opposite flow directions are seen near the inner and outer divertor targets. This behaviour is expected due to the opposite sign of B_z at the inboard and outboard sides of the divertor: the measurements are consistent with parallel impurity flows towards both targets. C III and He II impurities show an increase in $\bar{v}$ by a factor of 2–3 between L-mode and H-mode, while C II appears largely unchanged. The ability to image flows of different charge:mass ratio species in this way could provide insight in to the driving of the flows, e.g., thermal gradient and friction forces vs. electric fields.

C III data for the LSND plasma described above have been tomographically inverted to obtain impurity emissivity and $v_{||}$ profiles at 1 ms intervals over the entire current flattop of the discharge. Fig. 9 shows example reconstructed profiles for L-mode and ELMy H-mode (during an inter-ELM period) phases of the discharge. A large increase in C III flow

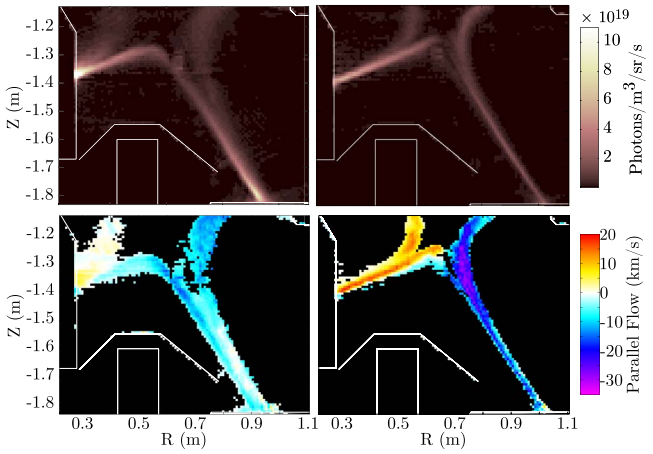

FIG. 9. Tomographically inverted C III (465 nm) emissivity (top) and $v_{||}$ (bottom) profiles in the lower divertor, in L-mode (left) and inter-ELM H-mode (right) phases of MAST single null divertor shot 29 541. Each emissivity/flow profile pair is obtained from a single 1 ms exposure.

This article is copyrighted as indicated in the article. Reuse of AIP content is subject to the terms at: http://scitationnew.aip.org/termsconditions. Downloaded to IP: 194.81.223.66 On: Tue, 16 Sep 2014 10:01:54

speed between L-mode and H-mode, as well as changes in the spatial flow structure are clearly seen in these images. A rectangular artifact is also seen in the intensity inversions at approximately $R = 0.65$ m, $Z = -1.3$ m, caused by a reflective in-vessel coil support which can also be seen in Fig. 8.

The C II and He II divertor data have proven less amenable to inversion than C III, due to the much brighter emission at the outer divertor strike point. Due to the divertor tile design on MAST this emission appears as a series of toroidally discrete bright spots in the images, as can be seen in Fig. 8. This causes artifacts in the emissivity inversions since these features are not consistent with the assumption of toroidal symmetry. Methods for accounting for this toroidal periodicity to improve the quality of these reconstructions are under development.

VII. SUMMARY

A coherence imaging impurity flow diagnostic has been developed for and operated on MAST, yielding images of C III, C II, and He II flows in the main scrape-off-layer and lower divertor. Time resolution up to 1 kHz and flow resolution of approximately 1 km/s have been achieved with spatial resolution better than 1 cm. The diagnostic has revealed novel carbon flow patterns in the high field side SOL under specific conditions, and wide angle divertor imaging shows differences between flows of different impurity species and between L and H modes. Tomographic inversion of the divertor data has been used to obtain C III $v_{||}$ profiles, while further work is required to obtain inversions for C II and He II.

ACKNOWLEDGMENTS

This work was part-funded by the RCUK Energy Programme under Grant No. EP/I501045 and the European Communities under the contract of Association between EURATOM and CCFE. The views and opinions expressed herein do not necessarily reflect those of the European Commission. SAS is funded by an EPSRC doctoral studentship. The Fusion Doctoral training Network is supported by EPSRC Grant No. EP/H012605/1. The authors thank Rutherford Appleton Laboratory for the loan of the Photron APX-RS camera used in this work.

[1]ITER Physics Expert Group on Divertor, ITER Physics Expert Group on Divertor Modelling and Database, and ITER Physics Basis Editors, Nucl. Fusion **39**, 2391 (1999).
[2]J. Howard, A. Diallo, M. Creese, B. D. Blackwell, S. L. Allen, R. M. Ellis, G. D. Porter, W. Meyer, M. E. Fenstermacher, N. H. Brooks, M. E. Van Zeeland, and R. L. Boivin, Rev. Sci. Instrum. **81**, 10E528 (2010).
[3]J. Howard, F. Glass, and C. Michael, Plasma Fusion Res. **2**, S1014 (2007).
[4]J. Howard, J. Phys. B: At. Mol. Opt. Phys. **43**, 144010 (2010).
[5]J. Howard, C. Michael, F. Glass, and A. Danielsson, Plasma Phys. Control. Fusion **45**, 1143 (2003).
[6]J. Howard, R. Jaspers, O. Lischtschenko, E. Delabie, and J. Chung, Plasma Phys. Control. Fusion **52**, 125002 (2010).
[7]M. Françon and S. Mallick, *Polarization Interferometers: Applications in Microscopy and Macroscopy* (Wiley-Interscience, 1971), pp. 21–24.
[8]J. Chung, R. König, J. Howard, M. Otte, and T. Klinger, Plasma Phys. Control. Fusion **47**, 919 (2005).
[9]K. Kato, IEEE J. Quantum Electron. **22**, 1013 (1986).
[10]S. Lawrence Marple, Jr., IEEE Trans. Signal Process. **47**, 2600 (1999).
[11]A. Andersen and A. Kak, Ultrason. Imaging **94**, 81 (1984).

This article is copyrighted as indicated in the article. Reuse of AIP content is subject to the terms at: http://scitationnew.aip.org/termsconditions. Downloaded to IP: 194.81.223.66 On: Tue, 16 Sep 2014 10:01:54